Solar wind predictions for the Parker Solar Probe orbit

Near-Sun extrapolations derived from an empirical solar wind model based on Helios and OMNI observations

M. S. Venzmer and V. Bothmer

University of Goettingen, Institute for Astrophysics, Friedrich-Hund-Platz 1, 37077 Göttingen, Germany

ABSTRACT

Context. In view of the planned near-Sun spacecraft mission Parker Solar Probe (PSP) (formerly Solar Probe Plus) the solar wind environment for its prime mission duration (2018–2025) and down to its intended closest perihelion (9.86 solar radii) is extrapolated using in situ data. The PSP mission will be humanity's first in situ exploration of the solar corona. Visiting this yet uncharted region is of special interest, because it will help answer hitherto unresolved questions on the heating of the solar corona and the source and acceleration of the solar wind and solar energetic particles. The solar wind extrapolation of this study is performed within the project Coronagraphic German And US Solar Probe Survey (CGAUSS) which is the German contribution to the PSP mission as part of the Wide field Imager for Solar PRobe (WISPR).
Aims. We present an empirical solar wind model for the inner heliosphere which is derived from Helios and OMNI in situ data. The German-US space probes Helios 1 and Helios 2 flew in the 1970s and observed solar wind in the ecliptic within heliocentric distances of 0.29–0.98 au. The OMNI database at NASA's Space Physics Data Facility consists of multi-spacecraft intercalibrated in situ data obtained near 1 au. The solar wind model is used together with sunspot number predictions to estimate the frequency distributions of major solar wind parameters PSP will encounter during its mission.
Methods. The model covers the solar wind's magnetic field strength and its plasma parameters proton density, velocity and temperature. Their individual frequency distributions are represented with lognormal functions. In addition, we also consider the velocity distribution's bi-componental shape, consisting of a slower and a faster part. The model accounts for solar activity and for solar distance dependency by shifting of these lognormal distributions. We compile functional relations to solar activity by correlating and fitting the frequency distributions with the sunspot number (SSN), using almost five solar cycles of OMNI data. Further, based on the combined data set from both Helios probes, the parameters' frequency distributions are fitted with respect to solar distance to obtain power law dependencies. Finally, by combining the found solar cycle and solar distance relations, we obtain a simple dynamical solar wind model for the inner heliosphere, confined to the ecliptic region.
Results. The inclusion of SSN predictions and the extrapolation to the PSP perihelion region enables us to estimate the solar wind environment for PSP's planned trajectory during its prime mission duration 2018–2025. The estimated solar wind values at PSP's nearest perihelion are: ... Their value vary up to 0.0000 %, arising only from differing amplitude assumptions for the next solar cycle.

Key words. solar wind – sun: heliosphere – sun: corona

1. Introduction

From observations of cometary tail fluctuations Biermann (1951) inferred the presence of a continuous flow of particles from the Sun. With his theoretical solar wind model Parker (1958) formulated the existence of the solar wind even before the first satellites measured it in situ in 1962 (Neugebauer & Snyder 1966, ref. to Russian measurements). The idea of a space mission flying through the solar corona dates back to the founding year of NASA in 1958 (STDT report, McComas2008). Since then several space missions have measured the solar wind in situ at a wide range of heliocentric distances, in the case of Voyager 1 as far away as 138 au[1], as of in July 2017, having even left the heliospause into interstellar space at a distance of about 121 au (Gurnett et al. 2013). Until today various spacecraft near Earth orbiting satellites have provided a wealth of solar wind measurements near Earth's orbit, with Wind (ref.), ACE (ref.) and DSCOVR (ref.) still orbiting around the L1 point 1.5 million km ahead of Earth in the sunward direction (ref. 1,2,3). Additional measurements at other distances were provided, e.g., by planetary missions to Venus and Mercury, such as PVO (ref.) or MESSENGER (ref.).

Ulysses was the first probe that orbited the Sun out of the ecliptic plane and thus could measured the solar wind at polar latitudes (McComas1998). The nearest in situ solar wind measurements to date were obtained by the US-German Helios mission.

[1] https://voyager.jpl.nasa.gov/

The in 1974 launched Helios 1 spaceraft reached distances of 0.31 au, Helios 2 launched two years later in 1976 and approached the Sun up to 0.29 au (Rosenbauer et al. 1977).

The NASA Parker Solar Probe (PSP), formerly Solar Probe Plus[1], spaceprobe with a planned launch date in mid 2018, will reach after six years in 2024 its closest perihelia at a distance of 9.86 solar radii (R_s), i.e. that is, 0.0459 au (Fox 2015 footnote 1: http://parkersolarprobe.jhuapl.edu/). This distance will be achieved through seven Venus gravity assists with orbital periods of 88–168 days. In its prime mission time 2018–2025 PSP provides 24 orbits with perihelia inside 0.25 au (Fox et al. 2015). It shall should be noted, that Even its first perihelion 88 93 days after launch in 2018, will take PSP to the an unprecedented region distance of 0.162 au, (i.e., 35.7 Rs). In comparison, the ESA Solar Orbiter mission with a planned launch in 2019 will have a closest perihelion of 0.289 au (ref.).

The key PSP science objectives are to "trace the flow of energy that heats and accelerates the solar corona and solar wind, determine the structure and dynamics of the plasma and magnetic fields at the sources of the solar wind, and explore mechanisms that accelerate and transport energetic particles" as stated in Fox et al. (2015). (NASA STDT report McComas2008). To achieve these goals, PSP has four scientific instruments on board: FIELDS for the measurements of magnetic fields and AC/DC electric fields (Bale2016), SWEAP for the measurements of flux of electrons, protons and alphas (Kasper2016), ISoIS for the measurement of solar energetic particles (McComas2016) and WISPR for the measurement of coronal and inner heliospheric structures (Vourlidas2016). (ref. to

each instrument paper).

The study presented in this paper is undertaken in the Coronagraphic German And US Solar Probe Survey (CGAUSS) project which is the German contribution to the PSP mission as part of the Wide field Imager for Solar PRobe (WISPR). The Wide field Imager for Solar Probe (WISPR) will contribute to the PSP science goals by deriving the 3D structure of the solar corona through which the in situ measurements are made to determine the sources of the solar wind. It will provide density power spectra over a wide range of structures (e.g., streamers, and pseudostreamers and equatorial coronal holes) for determining the roles of turbulence, waves, and pressure-balanced structures in the solar wind. It will also measure the physical properties, such as speed and density jumps of SEP-producing shocks and their CME drivers as they evolve in the corona and inner heliosphere (Vourlidas et al. 2016). In order to help optimize the WISPR and PSP preplanning of the science operations based on knowledge of the expected solar wind environment is needed. For this purpose the solar wind environment is extrapolated down to the closest perihelion of 9.86 R_s distance to the Sun using solar wind data from the Helios probes and near 1 au data from various satellites compiled in the NASA/GSFC OMNI solar wind database.

1.1 Solar wind

Generally, two types of solar wind are observed in the heliosphere, slow and fast streams (Neugebauer & Snyder 1966, Schwenn (19xx)). Slow solar wind has typical speeds < 400 km s^{-1} and fast solar wind has speeds > 600 km s^{-1} (see Schwenn1990, p.144). Their different compositions and characteristics indicate different sources and generation processes (McGregor et al. 2011b). Fast streams are found to originate from coronal holes as confirmed by Ulysses out-of-ecliptic polar measurements (McComas1998). The origin source of slow wind and its eventually different types (Schwenn19xx), is still a subject of controversial discussions because several scenarios are possible to explain its origin from closed magnetic structures in the solar corona, such as ...intermittent reconnection at the top of streamers and pseudostreamers, coronal hole boundaries, ... (ref.).

Their occurrence frequency of these slow and fast streams varies strongly with solar activity and their interactions lead to phenomena such as stream interaction regions (SIRs) and for quasi-stationary coronal source regions to co-rotating interaction regions (CIRs, ref. Buch über CIRs Balogh1999).

Superimposed on Embedded in the slow and fast solar wind streams are transient flows of coronal mass ejections (CMEs), the faster ones driving shock waves ahead (ref.). Their frequency rate follows the activity cycle and varies in near 1 au measurements between only one CME every couple of days during solar cycle minima up to multiple CMEs observed over several days at times of solar maximaum, that is, the CME-associated flow share of the solar wind raises from about 5% up to about 50% (Richardson & Cane 2012).

It is not known which specific solar wind type or structure PSP will encounter at a given time during its mission, therefore we extrapolate the parameters' probability distributions of the major solar wind parameters from existing solar wind measurements obtained near Earth orbit and by the two Helios probes at distances up to 0.29 au and takeing solar cycle dependences into account.

As a baseline we describe the solar wind environment through the four key quantities of a magnetized plasma: speed, density, temperature and magnetic field strength. Furthermore, the bulk flow solar wind velocity is the defining parameter of the two types of solar wind. The Solar wind quantities, like flux densities, mass flux and plasma beta, values can directly be derived from these four parameters.

##

We start with Our approach is to obtain an analytical representations of the shapes of the solar wind parameter's frequency distributions in section 2, investigate of their solar activity dependence in section 3 and perform of their solar distance scaling in section 4. The solar wind parameters' frequency distributions and solar activity dependence is derived from near-Earth solar wind and sunspot number (SSN) time series with a duration of almost five solar cycles. and Their distance dependency is derived from Helios solar wind measurements covering more than two third of the distance to the Sun between 0.29 and 0.98 au of and more than half a solar cycle by Helios 1 and 2 in 1974-198x.

From combination of the obtained frequency distributions, SSN dependence functions and solar distance dependence functions a general solar wind model is build established in section 5, representing the solar activity and distance behavior.

Finally, this empirical model is fed with a SSN prediction method proposed by NOAA/SWPC and extrapolated to PSP's planned orbital positions in section 6 in order to derive a most realistic solar wind scenario.

2. Frequency distributions of solar wind parameters

The solar wind parameters are highly variable, due to short-term variations from structures like slow and fast wind streams, interaction regions and CMEs, whose rate and properties depend on the phase of the solar activity cycle. Hence, for deriving characteristic frequency distributions for the solar wind parameters, measurements over long-term time spans are needed. The abundance of the near-Earth hourly OMNI data set is are ideally suited for this purpose because they it spans to date almost five solar cycles.

the phase of the solar cycle/activity.

The so-called OMNI 2 data set (King & Papitashvili 2005) hosted at NASA's Space Physics Data Facility (SPDF, http://omniweb.gsfc.nasa.gov/), Goddard Space Flight Center (GSFC) x combines intercalibrated solar wind plasma and magnetic field data collected by various satellites since the 1960s.

intercalibrated multi-spacecraft data which is time-shifted to the nose of the Earth's bow shock.
The data is obtained from the OMNIWeb interface[2] at N

For this study hourly data from 27 November 1963 until 31 December 2016 were used to derive the solar wind parameter frequency fits. It should be noted that the temperature data start after 26 July 1965. The data coverage of the parameters is in the range 67– 74 % corresponding to a time duration of 36–40 years.

————————————————

It should be noted that a test-comparison of hourly averaged with higher time resolution data for the time span 1981-2016, when these data are available, did not show significant differences.

The frequency distributions of the solar wind magnetic field strength, proton velocity, density and temperature are shown in Figure 1 for the investigated time period 1963-2016. According to the different data precisions we specified the bin sizes to 0.5 nT for the magnetic field strength, 10 km s^{-1} for the velocity, 1 cm^{-3} for the density and 10000 K for the temperature in order to have sufficient data in each bin representing the range of measured values. The solar wind magnetic field strength was in the range 0-40 nT, the velocity in the range 200-1.000 km/s, the density in the range 0-100 p/cm3, and the temperature in the range 5000-2 MK. These ranges are as expected statistically dominated by slow and fast solar wind streams, yielding frequency maxima around 4-5 nT, 370 km/s, 4 p/cm3 and 30000 K as expected from previous analysis of near 1 AU solar wind data (e.g., Table 3.3 in Bothmer and Zhukov 2007). Much lower or higher peak values at 1 AU have been observed in extraordinary events, such as the July 2012 ICME with a speed of over 2.000 km/s and a peak field strength of about 100 nT (Baker et al., 20xx) that was observed by STEREO A (but not at L1) or the so-called solar wind disappearance event observed in xxx (ref.).

Since all solar wind parameters have positive values we investigate how good the frequency distributions can be represented by lognormal functions using leastsquare regression fitting. The lognormal function is:

$$W(x) = \frac{1}{\sigma\sqrt{2\pi}x}\exp\left(-\frac{(\ln x - \mu)^2}{2\sigma^2}\right) \tag{1}$$

It depends on the location μ and the shape parameter σ. Changes in μ affect both the horizontal and vertical scaling of the function whereas σ influences its shape. The distribution's median x_{med} and mean x_{avg} (average) positions are straightforward to interpret and are directly calculated from μ and σ:

$$x_{med} = \exp(\mu) \iff \mu = \ln(x_{med}) , \tag{2}$$

$$x_{avg} = \exp\left(\mu + \frac{\sigma^2}{2}\right) \iff \sigma = \sqrt{2 \ln \frac{x_{avg}}{x_{med}}}. \tag{3}$$

It is apparent that the mean is always larger than the median. Re-placing the variables μ and σ with these relations, the lognormal function (1) becomes

$$\frac{1}{x\sqrt{}}\left(\ln^2\frac{x}{x_{med}}\right). \tag{4}$$

figures/histogram_fits_V_a_zoom_dbl_paper_pdfplot.pdf

Fig. 2. The velocity's frequency distribution (same as in Fig. 1) and its compositional lognormal fit. The fit's median and mean values and its two fit parts are indicated as well. The inset only has a zoomed-in frequency axis, its x-axis stays the same.

we combining two lognormal functions (4), involving more fit variables:

$$W_{II}(x) = c \cdot W_1(x) + (1 - c) \cdot W_2(x) . \tag{5}$$

The balancing parameter c ensures that the resulting function remains normalized as it represents a probability distribution.

The fitting of $W_{II}(x)$ to the velocity's frequency distribution yields the values of the five fit parameters c, $x_{med,1}$, $x_{avg,1}$, $x_{med,2}$ and $x_{avg,2}$ as listed in Table 1 together with the median and mean values of the composed distribution, which can be derived via solving the following equations:

$$\int W_{II}(x)\,dx = 0 \qquad \text{and} \qquad \int x\,W_{II}(x)\,dx = 0 \tag{6}$$

This fit function is more accurately

describing the velocity's frequency distribution as shown in Figure 2.

In this model the slow and fast part contribute almost equally ($c \approx 0.5$) to the long-term velocity distribution function. being valid for this kind

$$W(x) = \sqrt{2/\pi}\,\ln\frac{x_{avg}}{x_{med}}\,\exp\left[-4\left(\frac{\overline{x_{avg}}}{x_{avg}}\right)\right]$$

x_{med} The values of x_{med} and x_{avg} obtained from fitting the individual solar wind frequency distributions are listed in Table 1.

From visual inspection, the resulting curves describe well the shape of the magnetic field strength, density and temperature distributions as shown in Figure 1. However, for the solar wind velocity the fit function appears not to be as good in describing the measured distribution around its maximum and in the higher velocity range. This can be inferred directly from the sum of the absolute residuals (SAR) between data and fit listed in Table 1, being almost three times larger than those for the other parameters.

In order to find a better fit for the velocity distribution we assume that the velocity distribution can be made up of at least two overlapping branches (McGregor et al. 2011a). Therefore a compositional approach is chosen by

of long-term average. At different times in a solar cycle their contributions vary strongly.

For the bulk of the solar wind these static lognormal functions describe the parameters' distributions well, but can differ substantially in extreme events caused by CMEs.

It should be noted that the simple lognormal fit functions underestimate the distributions of the solar wind parameters in high value tails, except for the temperature's tail which is overestimated as seen by the inserted diagrams in Figure 1. The velocity's compositional lognormal fit only slightly overestimates its tail as seen also by the inserted diagram in inset in Figure 2.

3. Solar cycle dependence of the solar wind distribution functions

In the next step we investigate how the long-term solar wind distribution functions presented in section 2, depends on solar activity. Therefore we examine their correlation with the yearly sunspot number, being a commonly used long-term activity index provided by the online catalogue[3] at the World Data Center – Sunspot Index and Long-term Solar Observations (WDC-SILSO), Solar Influences Data Analysis Center (SIDC), Royal Observatory of Belgium (ROB).

Table 1. Resulting fit coefficients from the fitting of the lognormal function (4) to the shape of the solar wind near 1 au parameters' frequency distributions of OMNI hourly data. For the velocity also the fit parameters of the double lognormal function (5) are listed, as well as the median and mean values of the resulting velocity fit. The mean absolute errors and sums of absolute residuals are also listed. The values in brackets are the estimated standard deviations of each fit parameter.

x_{med}	Parameter		Mean^a	Balance	MAE		x_{avg}	c	[%]
	Magnetic field		6.164(18)	–	5.51 × 10^{-4}	6.83			
	Velocity		4.183(20)	–	1.80 × 10^{-3}	18.69			
	Density		6.484(34)	–	5.49 × 10^{-4}	6.48			
	Temperature		11.301(32	–	8.71 × 10^{-5}	5.78			
	Velocity W_1	4.89(14) 3.68(20)	5.00(14)	0.504(62)	–	–			
	W_{II} $_b$	4.16(14) $_b$	4.42(14)^b	–	3.98 × 10^{-4}	4.20			
	W_2		3.72(20)		–	–			

Notes. $^{(a)}$ Values in their respective units nT, 10^2 km s^{-1}, cm^{-3} and 10^4 K. $^{(b)}$ Error estimates derived from the individual fit part errors.

Fig. 1. Frequency distributions of the four solar wind parameters and their lognormal fits for the time period 1963-2016 derived from the hourly OMNI database. The histograms have bins of 0.5 nT, 10 km/s, 1 cm^{-3} and 10 000 K. The fit's median and mean values are indicated as well. The insered diagrams show zoomed-in frequency axes.

For this purpose we fit lognormal functions to the frequency distributions as in section 2, but implement linear relations to the yearly SSN allowing shifts of the distribution functions. For the velocity function the approach is different because two components are kept fixed and x their balance is modified with the changing SSN.

yet OMNI data are from Earth orbit, causing variations in solar latitude and distance. To dodge these seasonal variations we use yearly OMNI and SSN data.

Solar activity is commonly measured via the sunspot number. We want to correlate OMNI in situ measurements with the SSN,

---

[3] http://www.sidc.be/silso/

figures/OMNI_yearly_BVNTvsSSN_a.pdf

figures/OMNI_yearly_ssn_correlation_c_plot.pdf

Fig. 3. The solar wind parameter yearly medians derived from OMNI data and the yearly SSN from the SILSO World Data Center for the years 1963–2016. The solar cycle number is indicated. Their correlation coefficients with the yearly SSN are calculated for time lags back to -15 years (bottom).

Figure 3 shows yearly medians of the solar wind parameters for the years 1963-2016 and the yearly SSN together with the solar cycle number. The data are averaged to year values to avoid possible seasonal variations during the Earth's orbit around the Sun. The correlation coefficients of the solar wind parameters with the yearly SSN shown in the bottom part of Figure 3 were calculated for time lags back to -15 years to cover a time span longer than a solar cycle. The reason for using the median values is rooted in the nature of the lognormal function. As expected from previous studies, the solar wind velocity, density and temperature depend on the state of the solar cycle (e.g., Schwenn 1983, ref. zu Korrelationen), e.g., the fast solar wind is correlated with the presence of polar coronal hole

Fig. 5. Solar wind parameter median over lagged SSN. The yearly data medians (+) with their weighted linear fit (solid) are obtained from OMNI data. The error bars denote the SSN standard deviation and the relative weight of the yearly data coverage. The SSN dependent me- dian x is derived from the lognormal model fit (dashed line). For the velocity the median is derived from the SSN weighting of the slow and fast model parts, whose magnitudes are SSN independent (dotted line).

extensions to lower latitudes being a typical feature of the solar cycle, being the reason for the common velocity peak in the decreasing phase of the SSN, as pointed out e.g., by Bothmer and Zhukov (see Figure x, p.). Therefore the solar wind velocity, density and temperature maxima exhibit time-lags to the SSN maxima. Thus we derive the correlation coefficients for different time lags between solar wind parameters and SSN a shown in Figure 3.

The highest correlation coefficient of 0.728 to the SSN is found for the magnetic field strength which has no time lag. This finding is anticipated because the SSN is found to be directly proportional to the solar cycle evolution of the photospheric magnetic flux (Smith & Balogh 2003).

Velocity and temperature show a lag time of 3 years with peak correlation coefficients of 0.453 and 0.540. The density with a correlation coefficient of 0.468 has a lag of 6 years, which is in agreement with the reported density anticorrelation with the SSN by Bougeret et al. (1984).

As expected, the correlation coefficients' amplitudes of all parameters decline with increasing lag time and show a frequency of about 11 years.

To facilitate shifts of the solar wind frequency distributions with the SSN, we add a linear SSN dependency to the median

$$x_{\mathrm{med}}(ssn) = a_{\mathrm{med}} \cdot ssn + b_{\mathrm{med}} , \tag{7}$$

using a factor to the SSN a_{med} with a baseline b_{med}. We relate the mean with a scaling factor to the median to transfer its SSN dependency:

$$x_{\mathrm{avg}}(ssn) = (1 + a_{\mathrm{avg}}) \cdot x_{\mathrm{med}}(ssn) . \tag{8}$$

With the implementation of these relations into the lognormal function (4), the new dynamic fit function $W'(x, ssn)$ is then fitted to the yearly data. The three resulting fit coefficients (a_{med}, b_{med} and a_{avg}) are presented in Table 2.

As can be seen from Figure 4, naturally, the fit models match with the general data trends, though some single year variations are not x replicated by the model (e.g., the high velocity and temperature values in 1974, 1994 and 2003). The comparison with the yearly data median values over SSN shows that the medians obtained from the modelling have a quite similar slope as shown in Figure 5.

The solar wind velocity needs special treatment because of the double lognormal distribution (5). Since it is well known that slow and fast solar wind stream occurrence rates follow the solar cycle and basically maintain characteristic speeds (ref.) we keep the two velocity components' positions constant and just vary their balance with the SSN:

$$c(ssn) = c_a \cdot ssn + c_b . \tag{9}$$

The fit result (see Table 2) yielded a model in which three years after solar cycle minimum (SSN of zero) the contribution of slow solar wind to the overall solar wind distribution reaches a maximum value of about 66% and decreases with increasing SSN as shown in Figure 6.

To investigate the amount of slow and fast wind contributions depending on solar activity, we apply the commonly used constant veloc- ity threshold of $v_{\mathrm{th}} = 400$ km s^{-1} (cite?). The linear fit to the yearly data ratio and the derived model ratio show a good agreement (see Figure 6). ~~are quite similar~~

Table 2. Resulting fit coefficients from the OMNI data fitting with lagged SSN. For the velocity the fit parameters from the double lognormal fit and their balancing function are given. The values in brackets are the estimated standard deviation of each fit parameter.

Parameter	Median[a]		Mean[a]	Balance	
	SSN factor a_{med}	Baseline b_{med}	Scaling factor a_{avg}	SSN factor c_a	Baseline c_b
Magnetic field	$1.309(19) \times 10^{-2}$			$4.285(17)$	$8.786(78) \times 10^{-2}$
Density	$3.81(25) \times 10^{-3}$	$4.495(26)$	$3.050(27) \times 10^{-1}$	–	–
Temperature	$1.974(26) \times 10^{-2}$	$5.729(19)$	$6.541(28) \times 10^{-1}$	$-1.799(95) \times 10^{-}$	$0.638(32)$ –
Velocity W_1,	–	$3.633(12)$	$1.008(37) \times 10^{-2}$	3	
W_2,	–	$4.831(81)$	$2.31(20) \times 10^{-2}$		

Notes. [a] Values in their respective units nT, 10^2 km s^{-1}, cm^{-3} and 10^4 K.


Fig. 4. Solar wind parameter data frequencies, lognormal fit models with their median values (white) and the corresponding yearly SSN (grey) over the OMNI time period 1963–2016. The for the models shifted SSN is indicated by a black line. The velocity median is derived from the SSN weighted constant lognormal parts (dotted).

Specific velocity thresholds between slow and fast solar wind cannot be directly compared with the to some degree steeper balance parameters of the two fit functions used in this model. However, they appear being likely a more realistic approach than just taking specific velocity thresholds for the slow and fast wind in agreement with the overlapping nature of the velocity flows reported by McGregor et al. 2011a.

4. Solar distance dependency

In order to derive heliocentric distance dependence relationships of the solar wind distribution functions we apply power law fit func- tions to the Helios data which can be extrapolated to the PSP orbit in a subsequent step.

We use the fitting methods of section 3 for the set of distance-binned Helios 1 and 2 data. The Helios highly elliptical orbit in the ecliptic covered a solar distance range of 0.31–0.98 in case of Helios 1 and 0.29–0.98 au in case of Helios 2. Launched during solar cycle minimum, the data of both probes cover the rise to the maximum phase of cycle 21, covering 6.5 years at varying distances to the Sun.
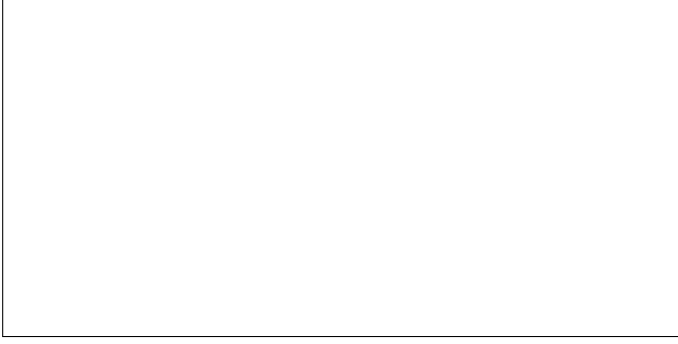
Fig. 6. **Ratio of** slow to fast solar wind during the solar cycle for a 3 years lagged SSN. The yearly ratios (+) and their weighted linear fit (solid line) are ob-tained from OMNI data with a threshold velocity of v_{th} = 400 km s^{-1}. The error bars denote the SSN standard deviation and the relative weight from the yearly data coverage. The model's balance parameter (9) and derived ratio (same threshold) are plotted as dashed and dotted lines.

In the same way as the OMNI data we investigate hourly averages of the Helios data. ~~It should be noted that Schwenn (1983) pointed out, that the hourly Helios data points which contain only a few measurements cause larger scatter to the Helios , nevertheless their effect is insignificant in the treatment of the bulk data.~~

The Helios 1 merged hourly data x from the magnetometer and plasma instruments (Rosenbauer et al. 1977) include 12.5 orbits for the time range 10 December 1974 until 14 June 1981, those for Helios 2 include 8.5 orbits for the time span 01 January 1976 until 04 March 1980. The data have been retrieved from the Coordinated Data Analysis Web (CDAWeb) interface at NASA's GSFC/SPDF[4].

The Helios 1 magnetometer data coverage for this data set is 43 %, (i.e., to 2.8 years), that of Helios 2 amounts to 54%, (i.e., to 2.3 years). The plasma data coverage is 76 %, (i.e., 5.0 years) in case of Helios 1 and 92 %, (i.e., 3.9 years) in case of Helios 2. Thus, x using this data, one has to keep in mind that its time coverage is unequally distributed over the solar cycle. The amount of data taken from shortly before solar cycle minimum in 1974 through the minimum in 1976 to the rising phase of the cycle in mid 1977, i.e. that is, to about 3 years before sunspot maximum in 1980, covers about 68 % of this period. From mid 1977 until 1981 data are available only 38 % of the time.

This is the reason why in this study the OMNI solar wind data have been used in section 2 to derive long-term frequency distributions for the key solar wind parameters and the study of its solar cycle dependency presented in section 3.

The median and mean values of the key solar wind parameters for different solar distances of the Helios data were calculated for the minimal distance resolution of the data set, which was! 0.01 au. Previous analyses have shown that the distance dependence of the solar wind parameters over the range of the Helios data from 0.29 to 0.98 au can be described well through power law scaling (e.g., Schwenn&Marsch, xxxx, Buch). Following, Schwenn ? we use the power function

$$x(r) = d\, r^e \tag{10}$$

for the regression fit of the median and mean, with r being the solar distance r. The fits are weighted through the different data counts per bin. With r in astronomical units we derive the fit coefficients listed in Table 3.

As expected, the velocity exponent derived for Helios 1 and 2 data found is basically the mean of the values found by Schwenn (1983, 1990), who derived the distance dependen- cies for both Helios spacecraft separately as $v_{H1}(r) \propto r^{0.083}$ and

as $v_{H2}(r)$ $r^{0.036}$. The difference in the exponents between Helios 1 and 2 have been attributed to the fact that the shorter Helios 2 data set is dominated by high speed streams. ?

The calculated density exponent agrees well with the Helios plasma density model derived by Bougeret et al. (1984), yielding a normalized 1 au density ($n(r) = 6.14$ $r^{-2.10}$ cm^{-3} for the year 1976. Those of the magnetic field strength and the temperature similarly agree with the studies by xxx and xxx.

Figure 7 shows the radial dependence of the solar wind parameters B, N, T and V over the distance range 0.29-0.98 au and the mean and median values and their respective power law fits. The mean and median velocity fits shown in Figure 7 are in agreement with the values listed in Table 3 are practically identical, so that the basic shape of the frequency distribution does not change with distance.

Contrary, the mean and median fits for the magnetic field strength cross each other at 0.339 au, in agreement with the Parker spiral geometry of the interplanetary magnetic field (IMF)?. Thus, the distribution function cannot well be described by a lognormal function. The fits for the proton temperature show a similar behavior, having an intersection at 0.082 au. Therefore the extrapolation of the magnetic field strength and proton temperature distribution frequencies to the PSP orbits by applying lognormal functions is limited. To circumvent such limitations we have set identically the exponents e_{med} and e_{avg} to identical values for all four investigated parameters. It should be noted that this simplification leads to slightly larger modelling errors, especially in case of the magnetic field strength.

Next we retrieved the frequency distributions of the four parameters in distance bins of 0.01 au, choosing the same resolution as for the OMNI data analyzed in section x – the distribution are plotted in Figure 8.

For simplification, as mentioned before, we treat the exponents of the median and average fit functions as being identical. Implementing the power law distance dependency (10) into the lognormal function (4), we get the fit Parameters $d_{m'ed}$, $d_{a'vg}$ and the common exponent e'. Again, we use the double lognormal function (5) for the velocity distri- bution fit, resulting in $W_{I'I'}(x, r)$. The additional fit parameters are the balancing parameter c' and for the second lognormal part $d_{m'ed,2}$ and $d_{a'vg,2}$. The resulting fit coefficients for the four solar wind parameters are presented in Table 4. The velocity balancing parameter $c' = 0.557$ is in good agreement with the results for the solar cycle dependency of the solar wind conditions derived from the analysis of the OMNI data presented in Figure 6.

The frequency distributions for the Helios solar wind parameter with respect to the radial distance from the Sun are plotted in Figure 8, together with the power law lognormal fits for B, N, T and double lognormal fits for the velocity V, including their median values.

Figure 8 shows that the fits represent the data well. The model's magnetic field strength is broader around values of 40 nT at the lower distance boundary than the frequency distribution implies. This behavior is expected because of the distance independent approximation applied. The velocity and temperature models' upper values, showing a higher frequency of these values than the actual data in agreement with the zoom boxes inserted in Figure 1.

This established solar wind model for the radial distance dependence is representative for the time of the Helios observations in solar cycle 21. The time variation of the exponents of the model fit functions are shown in Figure 9 together with the yearly SSN for the time period 1974-1982. From Figure 9 it can be seen that during this time period there is no clear variation of the exponents with solar activity.

figures/Vdbl_SSN_ratio_f_plot.pdf
~

Table 3. Fit coefficients for the median and mean solar distance dependencies of the four solar wind parameters for the combined Helios 1 and 2 data set. The errors in brackets are the estimated standard deviations of each fit parameter. The crossing distances indicate where the median and mean fits intersect each other. The year variation is the weighted standard deviation derived from all yearly fit exponents.

Parameter	Median		Mean		Crossing distance [au]	Year variation Δe
	d_{med}^{a}	e_{med}	d_{avg}^{a}	e_{avg}		
Magnetic field	5.3773(92)	−1.655(17)	6.05(10)	−1.546(18)	0.339(11)	0.11
Velocity	4.10710(28)	0.058(13)	4.356(24)	0.049(10)	0.7(83) ×	0.012
Density	5.61(27)	−2.093(46)	7.57(30)	−2.010(38)	0.027(73)	0.072
Temperature	7.14(23)	−0.913(39)	9.67(21)	−0.792(28)	0.082(85)	0.005

Notes. [a] In units of nT, 10^2 km s^{-1}, cm^{-3} and 10^4 K.

Fig. 7. Hourly Helios data of the magnetic field strength B, and the proton velocity V, density N and temperature T plotted for the solar distance range 0.29-0.98 au. The mean and median values per 0.01 au data bin and their fit curves are plotted as red and blue points and lines. To avoid distance gaps resulting from the 0.01 au binning, random distance values of ±0.005 au were added in this Figure.

Table 4. Fit coefficients from the single lognormal power function of B, N, T, and a double lognormal for the solar wind velocity derived from the combined Helios 1 and 2 data. The errors in brackets are the estimated standard deviations of each fit parameter.

Parameter	Median^{a} d'_{med}	Mean^{a} d'_{avg}	Exponent e'	Balance c'
Magnetic field	5.358(25)	5.705(28)	−1.662(11)	–
Density	5.424(33)	6.845(47)	−2.114(20)	–

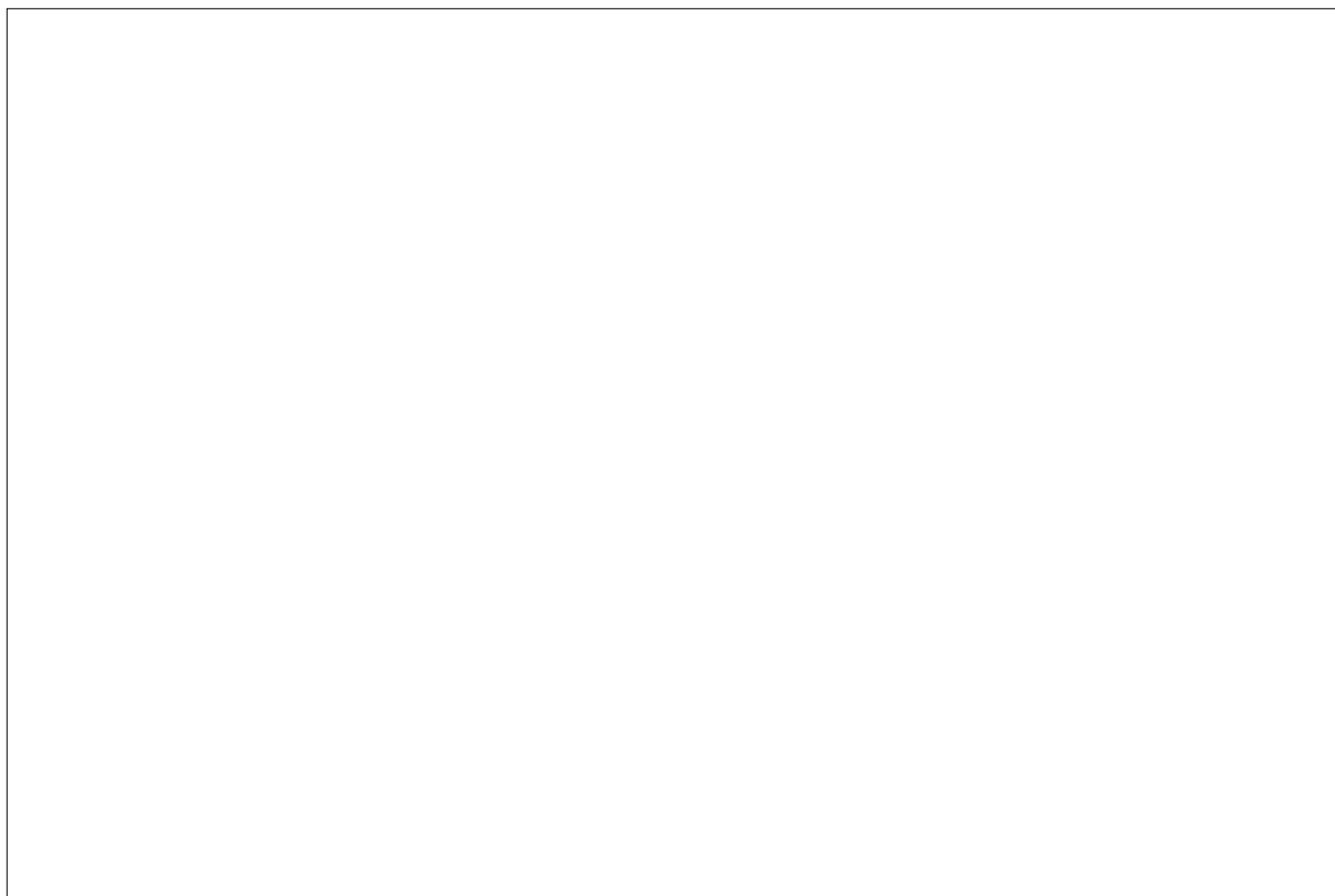|					
Temperature		6.357(64)	10.72(14)	−1.100(20)	–
Velocity	W_1''	3.707(13)	3.748(16)	0.0990(51)	0.557(45)
	W_2''	5.26(13)	5.42(11)		
	W_{11}''	4.13(13)[b]	4.47(11)[b]	–	–

Notes. [a]

figures/mixed_fit_fixed_4_paper_f_plot.pdf

Fig. 8. Solar wind parameter frequency distributions over solar distance. Plotted are the binned Helios data and the power law lognormal fit model (double lognormal for the velocity) with their median values (white). See text.

Fig. 9. Helios yearly variation of the solar wind parameters' fit exponents together with the SIDC 13-month smoothed monthly SSN. The year 1974 is omitted because of the Helios launch time.

For simplicity we assume, that the distance scaling laws can be treated as time independent through their mean values and use the calculated exponents' yearly variations summarized in Table 3 as relative uncertainties.

5. Empirical solar wind model

In order to derive the solar wind environment for the PSP orbit in the next steps we combine the results from the OMNI and Helios databases for the solar wind frequency distributions and their distance dependencies, taking into account the solar cycle relationship. The result will be an empirical solar wind model for the inner heliosphere which can then be extrapolated to the PSP orbit (section 6).

Since for the time interval of the Helios data no strong variations of the distance scaling laws was found, we combine in the next steps the frequency distribution of the solar wind parameters for 1 AU derived from the OMNI data and their median dependencies on the solar cycle with the exponents derived from the Helios data as presented in section 6:

$$x_{med}(ssn, r) = (a_{med} \cdot ssn + b_{med}) \cdot r^e, \quad (11)$$

Thus we obtain the combined model function $W'''(x, ssn, r)$

and , for the velocity function, with the double lognormal function: $W_{\text{I}'\text{I}''}(x, ssn, r)$ (5).

empirical model limits (spherical coordinates):
- heliocentric distance range 0.29–0.98 au

Fig. 10. PSP's solar distance during its mission time (top). Consecutive Venus flybys bring its perihelia nearer to the Sun. Actual and predicted SSN (bottom), that is, SIDC 13-month smoothed monthly actual SSN, SIDC prediction, SWPC prediction and simply by 11 years shifted SSN from previous cycle 24, together with two alternative trends of half and twice its amplitude.

6. Model extrapolation to PSP orbit

In order to derive the solar wind environment for the PSP orbit, finally the general solar wind model derived in the previous sections will be extrapolated to the PSP orbit, taking into account predictions of the SSN.

For the SSN short-term predictions several sources are available. The ROB SIDC provides 12-month SSN forecasts[5] obtained from different methods such as, e.g., the Kalman filter combined method. NOAA's Space Weather Prediction Center's (SWPC) method follows for the time period until end of 2019 the conclusions of the Solar Cycle 24 Prediction Panel[6]

For the prediction of the next solar cycle (i.e., cycle 25) we start by assuming a pattern similar to the last cycle and apply an 11 year shift to it. Additionally, we consider as possible alternatives a SSN pattern of half and twice its amplitude as shown in Figure 10. The SSN for PSP's first perihelion will be small—certainly below 20, whereas its closest perihelia reached end of 2024 and early 2025, should coincide with the end of its maximum phase.

---

[5] http://sidc.be/silso/forecasts
[6] http://www.swpc.noaa.gov/products/ solar-cycle-progression

Figure 10 includes the solar distances during the PSP mission beginning after launch in mid 2018. Parker Solar Probe is planned to launch in mid 2018. Seven Venus flybys will be used to decrease continually the perihel distances up to a minimum of 9.86 R_s (Fox et al. 2015). Science measurements by PSP are taken only at distances of 0.25 au and closer, the first perihel of PSP 88 days after launch in November 2018 will already take the spacecraft to 0.16 au.

For PSP's orbital range we extrapolate the derived solar wind distribution functions and compare the results with those from existing models as shown in Figure 11.

The magnetic field strength is found to increase from average values of about 40 nT at 0.25 au to 600 nT at 0.046 au for a SSN of 0. Taking a SSN of 200 increases the value to 60 nT at 0.25 au and 1000 nT at 0.046 au. Our extrapolation results are slightly flatter than those derived from the analytical magnetic field model by Banaszkiewicz et al. (1998), who constructed a dipole plus quadrupole plus current sheet (DQCS) model. This difference may have its origin in deviations of the real solar wind distribution function to the lognormal shape used for the extrapolation, but also can have its origin in the modelling approach.

The average velocity is found to decrease from 350 km/s at 0.25 au to about 290 km/s at 0.046 au for a SSN of 0. Whereas using a SSN of 200 it decreases from 390 km/s to 330 km/s. Comparing the results with those found by Sheeley et al (1997) and Wang et al. (2000) derived from …, who used LASCO coronagraph observations to track the slow solar wind originating in form of blobs from coronal streamers in the distance range 2–30 Rs, shows higher extrapolated velocity values near the PSP perihelia. However, generally it can be expected that PSP will encounter a slower solar wind environment close to the Sun and that it will truly measure solar wind acceleration processes as formulated in the Solar Probe STDT report (ref.) and stated by Wang et al. (2000).

The proton density increases from about 80 p/cm3 at 0.25 au to about 3.000 p/cm3 at 0.046 au, being almost independent of the SSN. The results are in good agreement with those of Leblanc et al. (1998) who derived an electron density model from type III radio burst observations. For the comparison we assumed that the number of protons and helium atoms is those of the electrons, with a helium abundance of 5 %. The Lebalanc et al. model shows that the density distance dependency scales with r^{-2} and steepens just below 10 Rs with r^{-6}.

The extrapolated proton temperature increases from about 200.000 K at 0.25 au to about 2 MK at 0.046 au for a SSN of 0 and from 400.000 K to 3 MK for a SSN of 200. Knowing that near-Sun coronal temperatures are in the range of 1-3 MK (ref.), the model obviously overestimates the extrapolated temperatures at this distance. The results can be compared to …

Taking the predicted SSN for the PSP mission time we finally estimated the solar wind environ- ment $W'''(x, ssn, r)$.

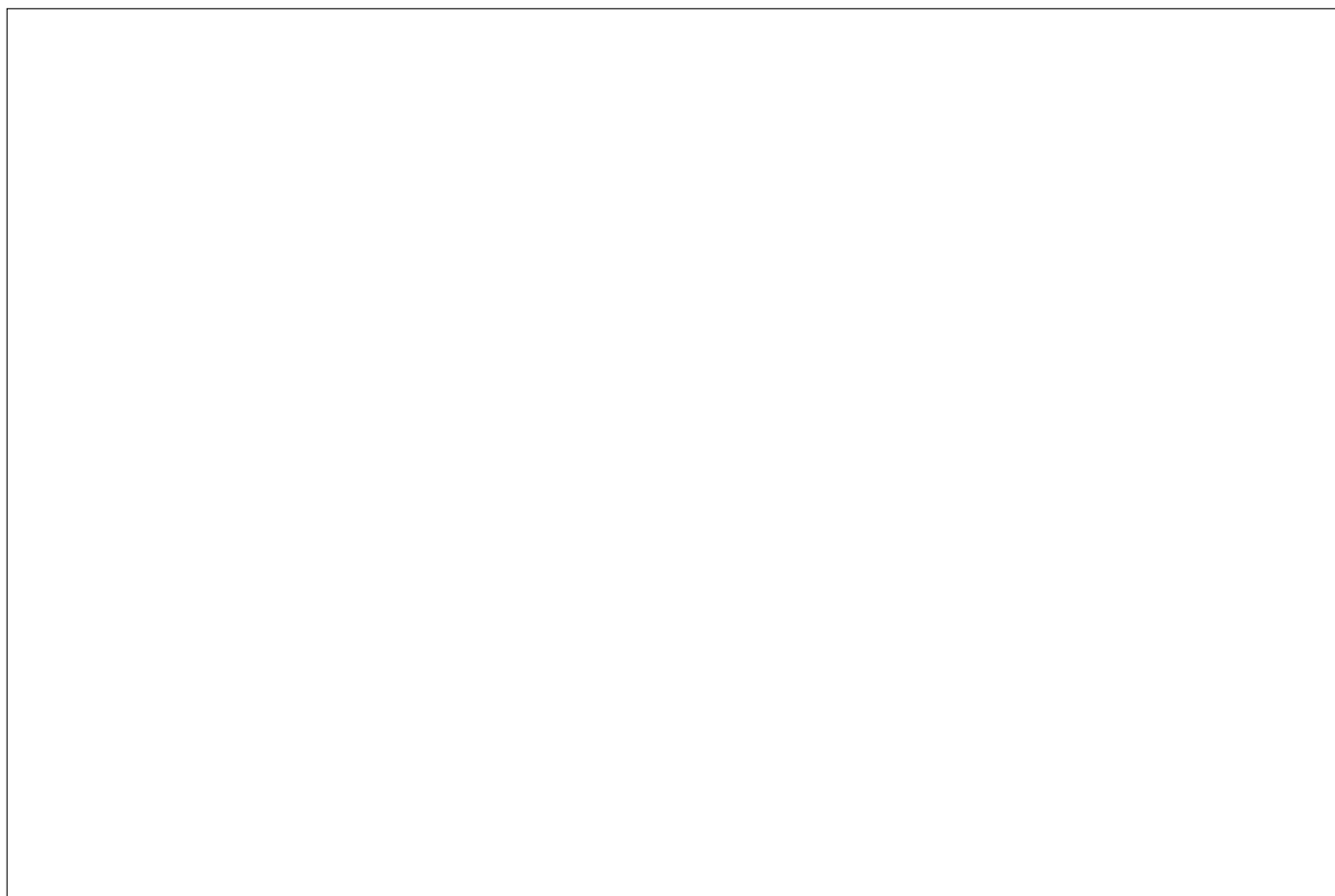figures/sw_extrapolation_ssn_b_plot.pdf

Fig. 11. Radial extrapolation of the solar wind parameters to the PSP orbit region. The from Helios and OMNI measurements obtained models are extrapolated to the PSP region—for the extreme cases of solar minimum (SSN = 0) and maximum (SSN = 200). Note that there is a time lag to the SSN depending on the solar wind parameter. The magnetic field radial dependence is slightly flatter than the analytic DQCS model for

solar minimum which Banaszkiewicz et al. (1998) derived. Below 20 R_s the slow wind velocity is overestimated in comparison to the measurements from Wang et al. (2000)) and (Sheeley et al. 1997). They derived temperature and sonic point values for slow solar wind with the isothermal expansion model (Parker 1958). Down to PSP's perihelion the density is in good agreement with the model from Leblanc et al. (1998). to 1-column...?

for the first and the nearest perihelia to infer which so- lar wind parameter magnitudes can be expected. Figures 12 shows the different parameters for 12 days comprising the first perihelion in Novemver 2018, Figure 13 shows the parameters for the closest perihelion in December 2024. In the beginning of the mission average peak values of about 90 nT, 340 km/s, 4000 p/cm3 and 500.000 K are estimated to be measured at 0.16 au (35.6 RS), increasing to about 1000 nT, 290 km/s, 10.000 p/cm3 and 2.000.000 K during the closest approach expected to happen in 2024 at 0.046 au (9.86 RS).
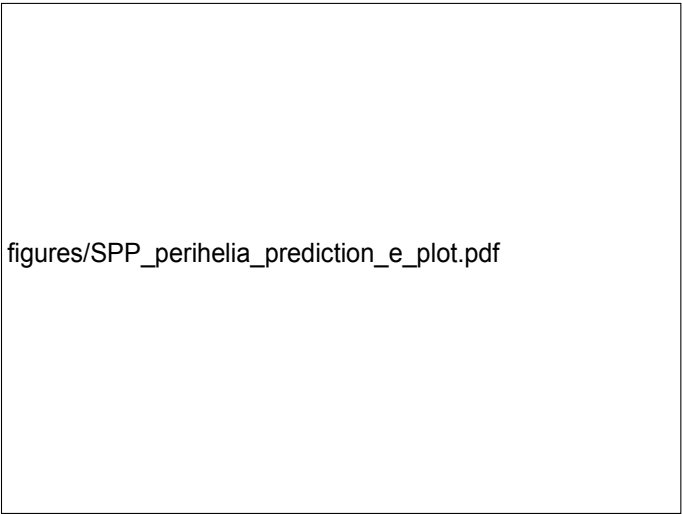
figures/SPP_perihelia_prediction_e_plot.pdf

Fig. 12. Estimated solar wind parameter medians (black) and their error bands (grey) during 12 days in 2018 with PSP's first perihelion at about 0.16 au. For the velocity the combined median is calculated and also the SSN independent slow and fast parts are plotted (dotted).

##
discuss high value zoom figures

figures/SPP_perihelia_prediction_nearest_e_plot.pdf

Fig. 13. Estimated solar wind parameter medians (black) and their error bands (grey) during during 12 days in 2024 with PSP's nearest perihe- lion at 0.0459 au. For the velocity the combined median is calculated and also the SSN independent slow and fast parts are plotted (dotted).

The solar wind parameters vary with solar distance as well as with latitudinal separation from the heliospheric current sheet (HCS).
The OMNI data is time-shifted to the nose of the Earth's bow shock. This leads to yearly solar distance variations of > 2 % (cite?) as the Earth orbits the Sun. Furthermore, its orbit within the ecliptic leads to a yearly variation of $7.2°$ in heliospheric latitude.
The HCS's position in latitude is highly variable around the solar equator (Schwenn 1990, p. 127 ff.?).

Error estimation over the year (seasonal/monthly) -> we expect variations to be less than 5 %

7. Discussion

list of results:
- empirical solar wind model for inner heliosphere within ecliptic
- low velocity at 0.0459 au
- slow/fast ratio SSN dependency
- application validity of lognormal distributions
–> B inversion of frequency distribution
—> magnetic field distribution's with distance increasing high value tail -> source are compression regions (why with density no increase?); look into Parker1958's B-field formula...
varying shape with distance is indicator for internal physical processes (mixing/turbulence...)

Balogh et al. (1999) p. 162 ff (origin and formation of CIRs in inner heliosphere with Helios data; latitude V dependence)
Balogh2009 (HMF review + inner heliosheath)
Aschwanden2004, p. 29
The near-Sun (PSP perihelion) solar wind velocity is expected to be slower than our model's estimates, because the position of the source (Alfvénic critical) surface is predicted to lie between 15–30 Rs (Schatten1969, Sittler1999, Exarhos2000, Katsikas2010, Goelzer2014; choose references...), up to which the solar wind is believed to be accelerated.

The Parker (1958) model of an isothermal expanding corona with a temperature of 10^6 K and a critical radius of 5.8 R_s.

individual velocity part discussion -> there is no specific velocity threshold between slow and fast solar wind types, the velocity ranges of both types overlap.
Not only the slowest wind but also the fastest wind is expected to converge to the average speed (Sanchez-Diaz2016 p.   2835,

using MHD-model -> very slow solar wind is continuation of slow wind) (because of interaction).

The ratio of both varies with solar activity, e.g., 3 years   after maximum, polar coronal holes are observed to often have equatorial extensions (cite?). see and use Bougeret et al. (1984) p. 498...

larger influx from higher latitudes (see figure b))

In most studies the density distance dependence is assumed
to scale with r^{-2} (cites), assuming a constant velocity.

Shifted to discussion:

validity and estimation of error size outside of valid model range…

derive heliocentric distance depending error...

list simplifications/approximations…

error estimation for general model and extreme value tendencies

error sources:
- extrapolation
- lognormal model
- SSN variance

all estimates outside these boundaries are extrapolations with large uncertainties.

8. Summary and conclusions

Further investigations should be done into structure extrapolations; outward extension of model to Mars seems feasable...

Further questions:
nearer to the Sun (at and below the source surface) the solar wind expansion in the ecliptic should be less spherical but more circular due to the influx from higher latitudes. **=>** density exponent **> -2**
see Li2011 Fig. 1

References

Balogh, A., Bothmer, V., Crooker, N. U., et al. 1999, Space Sci. Rev., 89, 141
Banaszkiewicz, M., Axford, W. I., & McKenzie, J. F. 1998, A&A, 337, 940
Biermann, L. 1951, ZAp, 29, 274
Bougeret, J.-L., King, J. H., & Schwenn, R. 1984, Sol. Phys., 90, 401
Feldman, W. C., Asbridge, J. R., Bame, S. J., & Gosling, J. T. 1978, J. Geophys. Res., 83, 2177
Fox, N. J., Velli, M. C., Bale, S. D., et al. 2015, Space Sci. Rev.
Gurnett, D. A., Kurth, W. S., Burlaga, L. F., & Ness, N. F. 2013, Science, 341, 1489
Kasper, J. C., Stevens, M. L., Korreck, K. E., et al. 2012, ApJ, 745, 162
King, J. H. & Papitashvili, N. E. 2005, Journal of Geophysical Research (Space Physics), 110, A02104
Leblanc, Y., Dulk, G. A., & Bougeret, J.-L. 1998, Sol. Phys., 183, 165
McGregor, S. L., Hughes, W. J., Arge, C. N., Odstrcil, D., & Schwadron, N. A. 2011a, Journal of Geophysical Research (Space Physics), 116, A03106
McGregor, S. L., Hughes, W. J., Arge, C. N., Owens, M. J., & Odstrcil, D. 2011b,
Journal of Geophysical Research (Space Physics), 116,
A03101 Neugebauer, M. & Snyder, C. W. 1966, J. Geophys. Res.,
71, 4469 Parker, E. N. 1958, ApJ, 128, 664
Richardson, I. G. & Cane, H. V. 2012, Journal of Space Weather and Space Climate, 2, A2
Rosenbauer, H., Schwenn, R., Marsch, E., et al. 1977, Journal of Geophysics Zeitschrift Geophysik, 42, 561
Schwenn, R. 1983, in NASA Conference Publication, Vol. 228, NASA Conference Publication
Schwenn, R. 1990, Large-Scale Structure of the Interplanetary Medium, ed. R. Schwenn & E. Marsch, 99

Sheeley, N. R., Wang, Y.-M., Hawley, S. H., et al. 1997, ApJ, 484, 472

SILSO World Data Center. 1963–2016, International Sunspot Number Monthly Bulletin and online catalogue ±

Sittler, Jr., E. C. & Guhathakurta, M. 1999, ApJ, 523, 812

Smith, E. J. & Balogh, A. 2003, in American Institute of Physics Conference Se- ries, Vol. 679, Solar Wind Ten, ed. M. Velli, R. Bruno, F. Malara, & B. Bucci, 67–70

Vourlidas, A., Howard, R. A., Plunkett, S. P., et al. 2016, Space Sci. Rev., 204, 83

Wang, Y.-M., Sheeley, N. R., Socker, D. G., Howard, R. A., & Rich, N. B. 2000, J. Geophys. Res., 105, 25133